Microwave Sensing of Yeast Cell Species and Viability

Jeffrey A. Osterberg, Neelima Dahal, Ralu Divan, Christina S. Miller, David Moline, Thomas P. Caldwell,
Xianzhong Yu, Sarah W. Harcum, and Pingshan Wang, *Senior Member, IEEE*

***Abstract*— We report the development of a simple interferometer-based microwave sensing system for multiple frequency characterization and differentiation of in-flow yeast cells. The interferometer uses a simple microstrip line, integrated with a microfluidic channel, for single-cell measurement. An algorithm was developed and verified with high-frequency structure simulator (HFSS) for complex permittivity, $\varepsilon^*(f) = \varepsilon'(f) - j\varepsilon''(f)$, extraction from measured scattering parameters. The sensing system and the algorithm were evaluated by measuring polystyrene particles of different diameters and at different interferometer operating frequencies. Viable and nonviable *Saccharomyces cerevisiae* and *Saccharomyces pastorianus* cells were measured at those frequencies. The results showed frequency-dependent permittivity values for each species of yeast and viability as well as frequency-dependent permittivity differences between different yeast types. The differences at some frequency points are significant and enable the differentiation of cells in mixed suspension, which is also demonstrated with a prediction model developed in this work.**

***Index Terms*— Brewing yeast, complex permittivity, cytometry, microwave sensing, single cell analysis.**

I. INTRODUCTION

MICROWAVE technology has attracted significant interest in biological cell sensing. It is highly sensitive, partly due to strong interactions between microwaves and cells and large permittivity contrasts between cells and liquid medium matrix. A variety of approaches have been developed and different types of cells have been tested. For instance, a combination of resonator and interference demonstrated high sensitivity microwave (1.1 GHz) detection of dual-frequency dielectrophoresis response of in-flow CHO cells [1]. A straight transmission line with a sensing gap has been used to monitor single-cell monocytes subject to electroporation [2], where a blocker is used to capture single cells for broadband measurement up to 40 GHz. A similar design was developed for detecting small populations of *E. coli* cells from 0.5 to 20 GHz [3]. Passive interferometers were built to measure single yeast cells [4]. Nevertheless, the lack of specificity has been the limiting factor for microwave cell sensing.

Results from various microwave and RF sensing efforts indicated potential measurement specificity. At lower frequencies, impedance measurements [5] have shown partial success in single-cell identification when the ratio of impedance at two different frequencies (i.e., opacity) is used [6], [7]. At 5 GHz, viable and nonviable yeast cells showed significantly different signals [4]. The fact that a cell species can have highly conserved and stable molecular components, such as fatty acids [8], likely enabled the differentiation due to differing charges, polarization, and dynamics of molecules of the bacteria. RF and microwave sensors have long been used for label-free sensing of cell suspensions due to their ease of construction and ability to take broadband measurements. Such sensors have been used to detect cancer cells (liver, breast, lymphocyte, bone) [21]–[26], on-line monitoring of cell adhesion [27], alterations of cell morphology and motility for cytotoxicity assessment of chemicals [28], and on-line biomass monitoring [29]. A major drawback of bulk measurements is the lack of insight provided on the large variability of individual cells within the population. Additionally, most studies of this type are well controlled in the lab and may not translate to real-world applications. These drawbacks could be overcome by measuring individual cells within a cell suspension over a broadband. Thus, a combination of broadband and high-frequency measurements of single cells presents the best opportunity in the search for cell differentiation power due to potentially added information of molecular relaxation not detected by single frequency or narrowband probing and cell organelles not detectable at low frequencies. As a result, microwave measurement specificity could be achieved without using bio-recognition elements or labels. The specificity would address the major limitation of microwave sensor application in biology as well as chemical and environmental monitoring, where substance identification is of paramount importance. While label-based technologies can provide high specificity, these tools are often labor- and cost-intensive.

Nevertheless, measuring single in-flow cells over a wide frequency range remains a challenge despite significant efforts and progress. In this work, we demonstrate the utility of

---

Manuscript received November 9, 2020; accepted November 16, 2020. Date of publication January 14, 2021; date of current version March 4, 2021. This work was supported in part by NSF under Grant 1711463 and Grant 1640578 and in part by the U.S. Department of Energy, Office of Science, Office of Basic Energy Sciences, for the use of the Center for Nanoscale Materials, an Office of Science user facility, under Contract DE-AC02-06CH11357. *(Corresponding author: Jeffrey A. Osterberg.)*

Jeffrey A. Osterberg, Neelima Dahal, David Moline, and Pingshan Wang are with the Holcomb Department of Electrical and Computer Engineering, Clemson University, Clemson, SC 29634 USA (e-mail: josterb@clemson.edu; pwang@clemson.edu).

Ralu Divan and Christina S. Miller are with the Argonne National Laboratory, Center for Nanoscale Materials, IL 60439 USA.

Thomas P. Caldwell and Sarah W. Harcum are with the Department of Bioengineering, Clemson University, Clemson, SC 29634 USA.

Xianzhong Yu is with the Department of Biological Sciences, Clemson University, Clemson, SC 29634 USA.

Color versions of one or more figures in this article are available at https://doi.org/10.1109/TMTT.2020.3048176.

Digital Object Identifier 10.1109/TMTT.2020.3048176

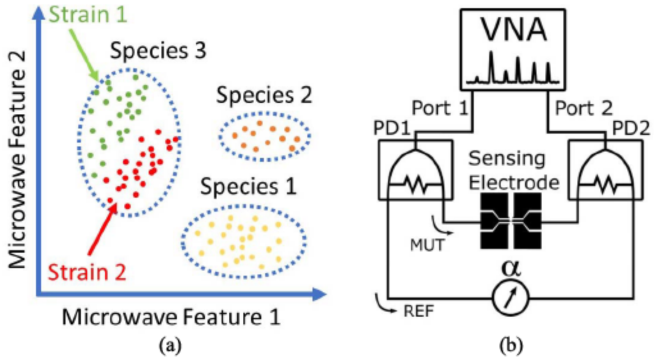

Fig. 1. (a) Illustration depicting the utilization of two microwave properties to identify/distinguish different species and strains. (b) Schematic of the simple tunable microwave interferometer used in this work for cell characterization. Two power dividers (PD) are used to split and combine the probing microwave signals and create interference between the two signal paths. MUT represents the MUT path, while REF represents the reference path. The attenuator, α, is used to balance the two paths to improve SNR ratio. A vector network analyzer (VNA) is used to generate and detect probing signals.

a simple tunable interferometer system for single-cell identification. When the tunable interferometer was applied to two brewing yeasts of closely related species, we showed significant microwave property differences that can be used to differentiate the species in a cell-particle mixture suspension. This article is arranged as the following: Section II describes the design considerations of the tunable interferometer for single-cell characterization at different frequencies. Section III reports the measurement results of live and dead cells from two brewing yeast species, *Saccharomyces cerevisiae* and *Saccharomyces pastorianus*. Section V discusses the project's findings and presents the conclusion.

II. TUNABLE MICROWAVE INTERFEROMETER FOR YEAST MICROWAVE SPECIFICITY INVESTIGATION

A significant number of single cells need to be measured over a wide frequency range for a microwave specificity analysis to identify species or other cell characteristics. Therefore, in-flow cell measurement, instead of measuring trapped cells, is necessary. Additionally, signal variations from various sources, such as cell position in the sensing zone, are required. Finally, the measurement system fluctuations should be small, much smaller than cellular heterogeneity within a cell species or strain, or smaller than intercellular differences for the analysis to be meaningful, as illustrated in Fig. 1(a). The measurement frequency should be tunable, since the frequencies that provide the best information for differentiation are unknown. At the same time, high-sensitivity measurements are necessary, since the difference between cells within a population is expected to be small. In this work, we choose a multifrequency tunable interferometer and examine two brewing yeast species.

Fig. 1(b) is a schematic of the interferometer device. The operating principle for this device has been described previously [9]. For this device setup, the sensing electrode is placed in the shorter path and an attenuator is used on the reference (REF) path to balance the loss between the two paths to maximize measurement signal-to-noise ratio (SNR).

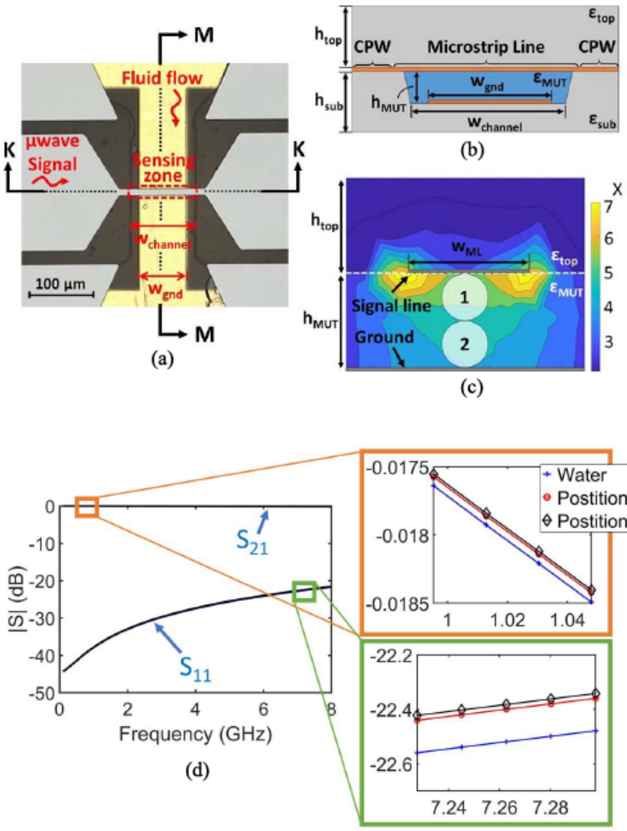

Fig. 2. (a) Top view of the sensing zone of the ML sensor. The microfluidic channel runs perpendicular to the microstrip and contains a ground plane along the base. (b) K–K cross section of the microfluidic channel showing the layers of the microstrip and the signal line transitions (CPW–ML–CPW). The sensing zone spans the width of the channel, w_{channel}, and is described by (6)–(10). The effects of the remaining sections of the sensor can be calibrated out using (3). The height (h_{top}) and dielectric constant (ε_{top}) of the top cover on the microstrip are 1 mm and 2.78, respectively. The height and permittivity of the lower substrate, labeled with the subscript sub, do not impact the behavior of the microstrip due to the placement of the ground plane at the base of the microfluidic channel, which acts as the lower substrate for the ML. Since the ML ground, w_{gnd}, is 80 μm wide and the channel is 100 μm wide, there are 10-μm gaps between the edges of the substrate ground and the edge of the channel, which adds some error both in the model and in measurements, since it is possible for a cell to miss the ground plane when passing under the ML. (c) M–M cross section of the microstrip showing the HFSS-simulated electric field intensity. The total electric field energy within two 4.5-μm-diameter spheres, one at the top of the channel (1) and one at the bottom (2), have a difference of 6%, showing that measurement error due to the vertical position of a cell is minimal. The cross sections in (b) and (c) are not to scale, since h_{top} and h_{sub} (both 1 mm) are over 100 times larger than h_{MUT}. (d) Broadband simulation of the ML section of the sensor for PSPs ($\varepsilon_r = 2.6$) in positions (1) and (2) using water as the reference material ($\varepsilon_{\text{MUT}} = 81$).

A. Microstrip Line as Sensing Electrodes

A simple microstrip line (ML), Fig. 2(a), was selected to be the sensing electrode in Fig. 1. Resonators can concentrate the probing fields and improve measurement sensitivity, such as measuring nanometer-scale cell membranes [10]. But their operating frequencies are limited and not easily tunable, thus inconvenient for frequency search/sweeping application. Coplanar waveguides (CPWs) are easier to build, yet the measurement signals are sensitive to cell position relative to CPW electrode surface [11], and the position is difficult to control. Hence, separating cell-intrinsic property variation from position variation in a measurement is challenging. For the ML arrangement in Fig. 2(a), it has better sensitivity than CPWs [12]. The interaction between a cell and the microwave fields varies with cell sizes and vertical location, Fig. 2(b), but the variations can be alleviated to likely tolerable levels by the use of larger *ML width,* w. Hence, the ML in Fig. 2 provides a reasonable tradeoff between sensitivity, field intensity variation, and frequency tunability.

The microstrip electrode in Fig. 2(a) is connected to a CPW transition section at each end. The use of CPW is for easier cable connections. The microfluidic channel, used to transport cell samples through the sensing zone, extends the width of the 10 mm × 10 mm sensor. The 500-μm-wide channel tapers to a width of 100 μm for a 250-μm-long section passing under the ML, giving a total channel volume of 43.6 nL. Microfluidic tubes inserted at the ends of the channel allow for samples to be injected via a syringe.

The sensor is made of two pieces—a top piece that serves as a cover for the microfluidic channel and contains the signal lines and the CPW ground plane, and a bottom piece that has the microfluidic channel, the microstrip ground, and four additional channels used to adhere the pieces. The sensors were fabricated on 4-in fused silica wafers using standard microfabrication processes. 20-Cr/200-Au metal was patterned using a liftoff procedure on both wafers to create the signal and ground lines. Five 9-μm-deep channels were etched in the bottom wafer, prior to metal patterning on the bottom wafer, by immersing in concentrated 49 wt% hydrofluoric acid (HF) for 10 min. Due to the relatively large etch depth, 5-Cr/100-Pt was used as masking material rather than more commonly used photoresists, since photoresist is easily penetrated by HF at high concentrations [17]. The microfluidic channel, labeled w_{channel} in Fig. 2(a), runs perpendicular to the signal line at the center of the sensor. The other four channels are used to adhere the two pieces together using optical glue. The glue channels are each 200 μm wide and span the width of the sensor. The bases of the channels are metal coated to create a ground plane for the microstrip and ensure continuity of the CPW ground. The width of the microstrip ground, w_{gnd}, is slightly narrower than the microfluidic channel at 80 μm to allow for misalignment during fabrication. The areas above the channels on the top wafer are left transparent to allow for viewing under a microscope. After adhering the signal and ground pieces, tubes are inserted into drilled holes at the ends of the microfluidic channel, allowing continuous fluid flow through the sensor. The final assembled device is mounted in a brass assembly with SMA connectors, shown in Fig. 3(b). Fig. 4(b) shows the broadband measurement and simulation results of the ML. There was very good agreement between measured and simulated $|S_{21}|$ over the entire operating frequency range and $|S_{11}|$ agrees well below 6 GHz. The differences above this are likely due to effects from the connectors, optical glue, and device imperfections from fabrication, particularly scratches created from drilling the microfluidic channel inlets, being difficult to account for in the simulation.

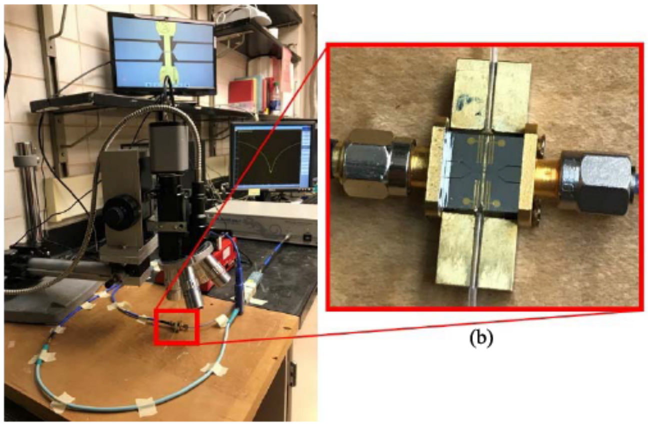

(a)

Fig. 3. (a) Benchtop assembly showing the interferometer setup with VNA, microscope, and (b) final assembled ML sensor.

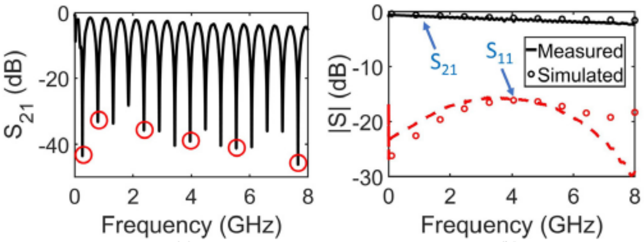

(a) (b)

Fig. 4. (a) Broadband measurement of the interferometer in Fig. 1(b) with an ML. Yeast measurements were taken at the six frequencies circled. (b) Comparison of measurement and simulation results for the sensing electrode over the operating frequency range.

With the ML in the interferometer in Fig. 1(b), the path lengths were fixed such that the interferometer had a fundamental frequency of 265 MHz, with harmonics approximately every 530 MHz, as shown in Fig. 4(a). This allowed for easy switching between operating frequencies over a wide range of frequencies. A tunable phase shifter could be added in series with the attenuator if increased frequency tunability is desired.

B. Cell Permittivity Extraction

In order to obtain cell permittivity information, $\varepsilon^*(f) = \varepsilon'(f) - j\varepsilon''(f)$, from measured S-parameters, we first extract the effective substrate permittivity of the ML sensing zone section. The ML propagation constant, $\gamma = \alpha + j\beta$, can be obtained from the measured S_{21}. The output at port 2 of the interferometer in Fig. 1(b) is [9]

$$S_{21} = A_{\text{MUT}} e^{-\gamma_{\text{MUT}} l_{\text{MUT}}} + A_{\text{REF}} \tag{1}$$

where the subscript MUT and REF refer to the material under test and the reference material, respectively. The complex constants A_{MUT} and A_{REF} are the normalized transmission coefficients of the two paths. The transmission coefficient of the ML sensing zone is described by the term $e^{-\gamma_{\text{MUT}} l_{\text{MUT}}}$. These constants can be eliminated by using two calibration liquids with known propagation constants by

$$\frac{S_{21\text{MUT}} - S_{21\text{cal1}}}{S_{21\text{cal2}} - S_{21\text{cal1}}} = \frac{e^{-\gamma_{\text{MUT}} l_{\text{MUT}}} - e^{-\gamma_{\text{cal1}} l_{\text{cal1}}}}{e^{-\gamma_{\text{cal2}} l_{\text{cal2}}} - e^{-\gamma_{\text{cal1}} l_{\text{cal1}}}} \tag{2}$$

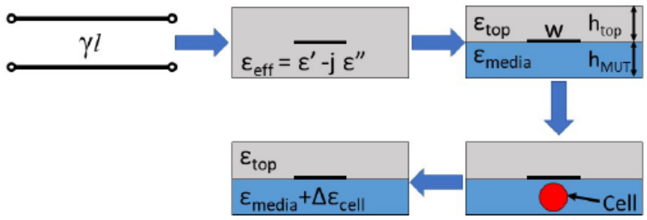

Fig. 5. Cell permittivity determination process. The schematic starts at the transmission line model. The parameter γl is calculated from S_{21} using (2). This parameter is used to obtain $\varepsilon^*_{\text{eff}}$, which describes the permittivity of a microstrip if it were surrounded by a homogeneous medium. Equations (6)–(10) are used to determine the media permittivity, $\varepsilon^*_{\text{media}}$, prior to cell measurements, where a cell is represented by the circle. The thickness and permittivity of the glass cover, h_{top} and ε_{top}, the channel height, h_{MUT}, and the electrode width, w, are constants defined by the device geometry and materials. When a cell passes under the electrode the overall MUT permittivity changes, labeled as $\Delta\varepsilon^*_{\text{cell}}$.

where the cal1 and cal2 subscripts refer to the signals from two calibration solutions. Solving for $\gamma_{\text{mut}} l_{\text{mut}}$ gives

$$\gamma_{\text{MUT}} l_{\text{MUT}} = \ln\left[\left(\frac{S_{21\text{MUT}} - S_{21\text{cal1}}}{S_{21\text{cal2}} - S_{21\text{cal1}}}\right)\left(e^{-\gamma_{\text{cal2}} l_{\text{cal2}}} - e^{-\gamma_{\text{cal1}} l_{\text{cal1}}}\right) - e^{-\gamma_{\text{cal1}} l_{\text{cal1}}}\right]. \quad (3)$$

The effective complex permittivity is then determined from γ_{mut} by [35]

$$\varepsilon_{\text{eff}} = \frac{\beta^2 - \alpha^2}{\omega^2 \mu_0 \varepsilon_0} \quad (4)$$

and

$$\varepsilon''_{\text{eff}} = \frac{2\alpha\beta}{\omega^2 \mu_0 \varepsilon_0}. \quad (5)$$

This results in the effective permittivity of the microstrip portion of the sensor, which assumes a homogeneous medium surrounding the microstrip (Fig. 5).

The next step is to use this measured effective permittivity to determine the relative permittivity of the medium. The above analysis is valid for any sensor in an interferometer system, provided the impedance changes during measurements are small enough that reflections can be ignored. Extracting the permittivity of the medium from the effective permittivity, however, is dependent on the device geometry.

Closed-form solutions based on the conformal mapping are commonly used to relate effective and relative permittivity of microstrip devices; however, these models are typically intended for single-layer microstrips. For multilayered structures, curve fitting techniques can be used, but this is a difficult endeavor. Due to the multilayer structure of the microstrip and the large permittivity of the mediums we found the variational method in the Fourier domain, along with the transverse transmission line (TTL) technique [14], to be more accurate than conformal mapping based models and more computationally efficient compared to full-wave electromagnetic methods. Since the ML is embedded in an inhomogeneous medium the propagating mode is approximated as quasi-TEM, for which the effective permittivity is related to the capacitance by [18]

$$\varepsilon^*_{\text{eff}} = \frac{C^*}{C_0} \quad (6)$$

where C^* is the capacitance of the multilayered ML per unit length and C_0 is the capacitance of the ML with the dielectric layers replaced by air. The capacitance of the ML can then be determined from the variational expression of line capacitance in the Fourier domain [13]

$$\frac{1}{C^*} = \frac{1}{\pi}\int_0^\infty \left[\frac{\tilde{f}(\beta)}{Q}\right]^2 \tilde{G}(\beta, h)\, d\beta \quad (7)$$

where $\tilde{f}(\beta)$ is the charge distribution in the Fourier domain where total charge Q on the center conductor, per unit length, is

$$\frac{\tilde{f}(\beta)}{Q} = \frac{8}{5}\left[\frac{\sin(\beta w/2)}{(\beta w/2)}\right] + \frac{12}{5(\beta w/2)^2} \times \left[\cos(\beta w/2) - \frac{2\sin(\beta w/2)}{(\beta w/2)} + \frac{\sin^2(\beta w/4)}{(\beta w/4)^2}\right] \quad (8)$$

where w is the width of the microstrip. $\tilde{G}(\beta, h)$ is the Green's function in the Fourier domain, defined as [14]

$$\tilde{G}(\beta, h) = \frac{1}{\beta Y^*} \quad (9)$$

where the Y-admittance parameter for a two-layer microstrip is given by [19]

$$Y^* = \varepsilon^*_{\text{MUT}} \coth(\beta h_{\text{MUT}}) + \varepsilon^*_{\text{top}}\left\{\frac{\varepsilon^*_{\text{top}} + \coth(\beta h_{\text{top}})}{1 + \varepsilon^*_{\text{top}} \coth(\beta h_{\text{top}})}\right\} \quad (10)$$

where h_{top} (1 mm) and h_{MUT} (9 μm) are the substrate and channel thicknesses, respectively, and ε_{top} is the dielectric constant of the glass substrate.

So, the effective permittivity, $\varepsilon^*_{\text{eff}}$, is determined from S-parameter measurements using (1)–(5), then $\varepsilon^*_{\text{MUT}}$ is obtained using look-up tables. Due to the complexity of (7) there is no closed-form expression for $\varepsilon^*_{\text{MUT}}$, so look-up tables were used to determine $\varepsilon^*_{\text{MUT}}$ from the measured $\varepsilon^*_{\text{eff}}$. Equations (6)–(10) were used to generate two tables, one relating $\varepsilon'_{\text{MUT}}$ and $\varepsilon'_{\text{eff}}$, and one for $\varepsilon''_{\text{MUT}}$ and $\varepsilon''_{\text{eff}}$, by sweeping one of the values of $\varepsilon^*_{\text{MUT}}$ (real or imaginary), and calculating the corresponding part of $\varepsilon^*_{\text{eff}}$. The maximum error created by using the tables was found to be less than 0.01% for ε' and less than 0.5% for ε''. The permittivity extraction process is summarized in Fig. 5. When a cell passes under the electrode the overall MUT permittivity changes. Throughout this article when discussing $\Delta\varepsilon^*_{\text{cell}}$ we are referring to the peak change in permittivity, which occurs when the cell is centered under the electrode.

To validate the model described in (6)–(9), the effective permittivity $\varepsilon^*_{\text{eff}}$ was calculated from relative permittivities $\varepsilon^*_{\text{MUT}}$ and compared with simulation using ANSYS high-frequency structural simulator (HFSS). The ML was simulated by sweeping the real and imaginary parts of $\varepsilon^*_{\text{MUT}}$ and calculating $\varepsilon^*_{\text{eff}}$ using (4) and (5), and the propagation constant γ from HFSS. The simulated and calculated values for $\varepsilon^*_{\text{eff}}$ are plotted in Fig. 6.

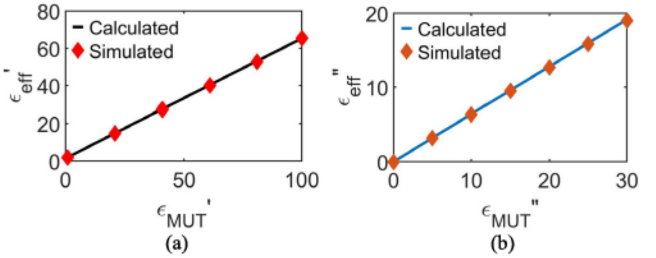

(a) (b)

Fig. 6. Calculated and simulated (a) $\varepsilon'_{\text{eff}}$ and (b) $\varepsilon''_{\text{eff}}$ for values of $\varepsilon'_{\text{MUT}}$ and $\varepsilon''_{\text{MUT}}$ for the ML. The permittivity extraction model described in (6)–(10) shows good agreement with HFSS simulation.

III. Yeast Measurements

The microwave interferometer system is shown in Fig. 1(b) and the algorithms were evaluated first using polystyrene particles (PSP) with various diameters (3 to 7.3 μm). The measurements taken using the PSP were used to determine the sensor accuracy, sensitivity, and precision. The second evaluation of the microwave interferometer system probed viable and nonviable *S. cerevisiae* and *S. pastorianus*, two popular species of yeast used in the production of beer, for signal characteristics.

The two species are nearly identical in size and shape, which makes visual identification difficult [36], [39]. Both are elliptical in shape and vary from 7 to 10 μm long and 4 to 7 μm wide [37], [38]. The similar morphologies are a result of *S. pastorianus* being a hybrid *S. cerevisiae* and another species, *S. eubayanus*, which also gives *S. pastorianus* a double size genome [36], [44], [45]. As such, biochemical techniques such as mass spectrometry and polymerase chain reaction (PCR) must be employed to identify closely related species [40]–[42]. These techniques are expensive and time consuming. The ability to rapidly distinguish between similar species such as these could provide a valuable new methodology for microbiologists.

When yeast from either species is killed by heat shock there is no noticeable change in morphology, provided the temperature is not so high to completely breakdown the cell membrane. Nonetheless, high temperature and subsequent cell death are known to increase membrane permeability [44]. Consequently, there were no visual differences between the two yeast species and the two states for each condition (live and dead). Thus, the differences in microwave properties were due to the inherent differences between the cells.

A. System Evaluation With PSP

Five spherical polystyrene microparticles with diameters—3, 4.4, 5.5, 6.2, and 7.3 μm were suspended in DI water and pumped through the sensor at a rate of 20 μL/h using a syringe pump to obtain signals for the six targeted frequency points shown in Fig. 4. These frequencies were 7.65, 5.55, 3.96, 2.38, 0.800, and 0.265 GHz. When a particle passed under the ML, a shift in S_{21} was observed, which corresponded to a change in the complex permittivity due to the permittivity contrasts between the cell/particle and medium.

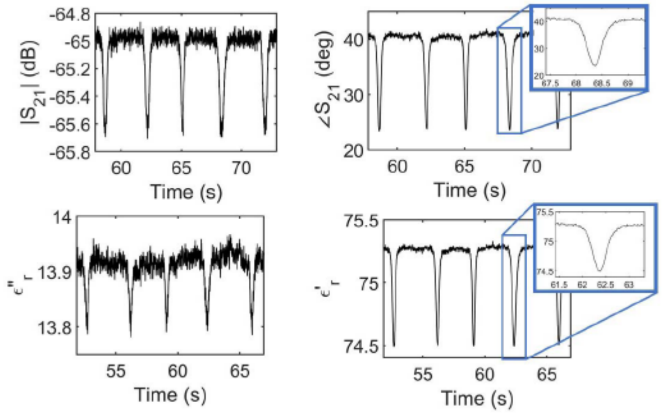

Fig. 7. Multiple measurements of a single 5.5-μm particle at 3.96 GHz. The same particle was manually controlled to pass back and forth across the sensing electrode to test the repeatability of the measurement. The particle position was controlled by first injecting the particle solution into the sensor and waiting several minutes until the particles stopped moving. The particle's lateral position can then be precisely controlled by raising and lowering the tubes connected to the inlet. The average shifts of ε' and ε'' were 0.760 ± 0.013 and 0.145 ± 0.006, respectively. The differences between measurements can be attributed to noise having a small effect on the peak shift value.

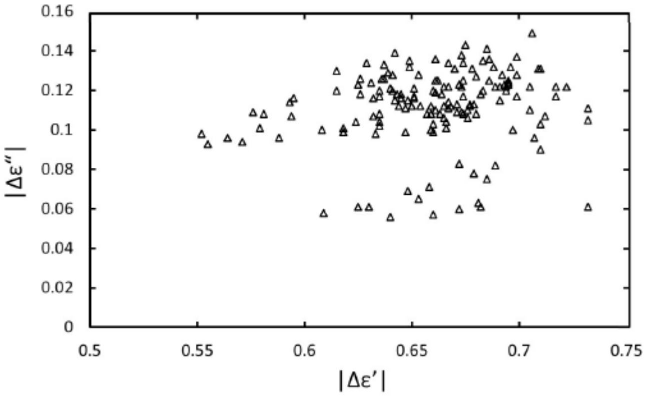

Fig. 8. Scatter plot of permittivity shifts for 150 5.5-μm PSP particles measured at 3.96 GHz.

Fig. 7 shows a typical S_{21} signal and the corresponding permittivity change with DI water as the background reference. The signals are obtained with the same particle that passes through the sensing electrode multiple times. The measurement time step is approximately 10 ms. The average shifts of ε' and ε'' were 0.760 ± 0.013 and 0.145 ± 0.006, respectively. The results show that the setup in Fig. 1(b) is sensitive and the measurements are repeatable.

Fig. 8 shows the measured results of 150 5.5-μm PSP particles measured one at a time. The average shifts for all the particles are 0.660 ± 0.044 (ε') and 0.112 ± 0.022 (ε''). The coefficients of variation of $\Delta\varepsilon'$ and $\Delta\varepsilon''$ are 5.40% and 17.53%, respectively. Compared to 13.64% particle volume variation, the system has good measurement accuracy.

Fig. 9(a) shows measured S_{21} of PSPs with different diameters. The minimum detectable PSP particle and permittivity change, which yields an SNR of 3:1, is frequency-dependent as shown in Fig. 9(b). The sensitivity decreases

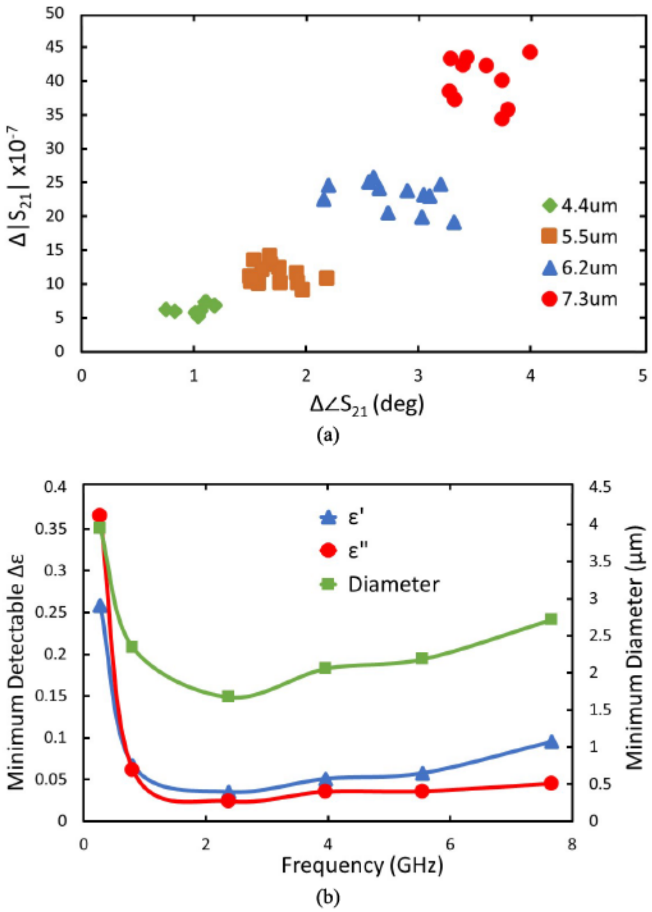

(a)

(b)

Fig. 9. (a) Scatter plot of the observed S_{21} shift for various sizes of microparticles at 1.81 GHz. Each point represents the peak induced shift, plotted as magnitude versus phase. (b) Minimum detectable shift in permittivity and minimum detectable PSP diameter for a 3:1 SNR.

at lower frequencies due to decreasing electrical length. At higher frequencies, the sensitivity flattens out because of increased sensitivity to mechanical noise in the cables. The predicted smallest measurable PSP particle is 1.7 μm diameter, assuming a linear relationship between volume and signal size, which would occur at 2.38 GHz.

B. Yeast Cell Measurement

S. cerevisiae and *S. pastorianus* cells, shown in-flow in the sensor in Fig. 10, were grown in Yeast Extract-Peptone-Dextrose (YPD) medium until a concentration greater than or equal to 10^6 cells/mL was reached, typically around 24 h.

The cells are diluted 40:1 DI water:cell medium immediately before taking measurements. Since measurements are taken for individual cells, we are not concerned with the consistency of the cell concentrations between measurements, but rather the consistency of the medium since that will affect the baseline permittivity. Dead cell samples are obtained by killing yeast in 90 °C water for one minute. The effectiveness of the methods used for cell growth and killing the cells was confirmed by performing cell viability counts using Trypan blue and a hemocytometer. We found *S. cerevisiae* live samples are at least 97% viable and dead samples contain less than 1% viable cells and *S. pastorianus* live samples are over 99% viable and dead samples have less than 2% viable cells. All samples were prepared to be as uniform as possible to keep the baseline permittivity constant throughout measurements. However, due to the complex biological processes taking place during cell growth, there will always be slight differences in the media. We found the solution media permittivity had a maximum standard deviation between measurement samples of 0.9 for ε' and 0.3 for $\varepsilon,''$ occurring at 0.265 and 0.8 GHz, respectively, and the percent difference between media permittivities was less than 3% for all frequencies except for ε'' at the same two frequencies, although the larger differences are exaggerated due to the small values of $\varepsilon.''$ The effects of these differences are minimal compared to the intrinsic differences between cells within a given population.

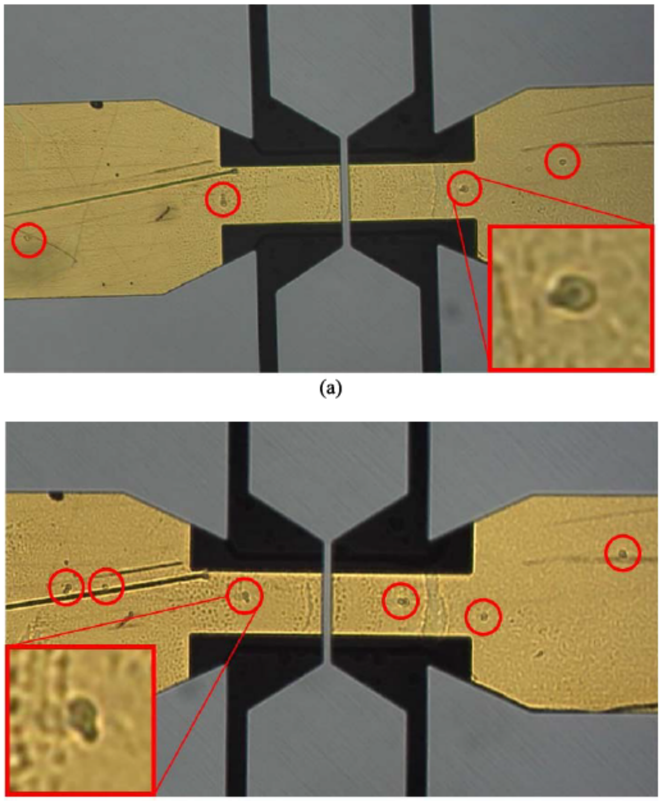

(a)

(b)

Fig. 10. Microscope images taken of live (a) *S. cerevisiae* and (b) *S. pastorianus* cells in-flow. The two strains, whether alive or dead, are visually indistinguishable.

Multiple time-domain measurements are taken of four yeast samples, including two yeast species, *S. cerevisiae* and *S. pastorianus,* at two physiological states, live and dead. Measurements were taken one frequency at a time under the assumption that the solutions have a uniform distribution (i.e., uniform baseline). Fig. 11 shows typical measurement results of *S. pastorianus* cells at 2.38 GHz. Each signal represents a cell passing under the ML, with the peak change in ε' and ε'' occurring when the cell is under the center of the electrode.

Scatter plots for three of the six frequencies are shown in Fig. 12. Each point in the plots represents the absolute value of the difference between the average baseline value and the peak change in both ε' and ε'' for a single cell.

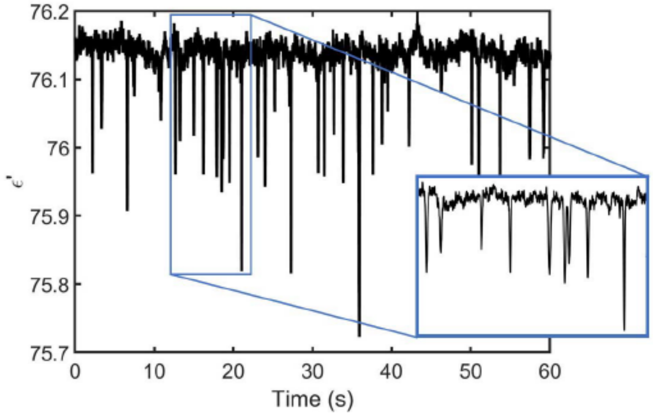

Fig. 11. Typical time-domain measurement of *S. pastorianus* yeast cells, taken at 2.38 GHz. Each signal is due to a single cell passing through the sensor. The S-parameter data are used to calculate the complex permittivity, then the peak change in ε' and ε'' is used to obtain the cell population's response, shown in Fig. 12, where each point represents the peak change in both ε' and ε'' for a single cell.

TABLE I

COEFFICIENTS OF VARIATION OF $\Delta\varepsilon'$

Frequency (GHz)	SC Live	SC Dead	SP Live	SP Dead	5.5 µm
7.65	58.2%	61.1%	41.2%	51.4%	5.06%
5.55	42.1%	47.4%	41.7%	49.3%	3.78%
3.96	51.9%	57.3%	45.3%	51.0%	5.40%
2.38	43.2%	50.1%	38.9%	52.50%	4.78%
0.80	57.8%	50.6%	38.9%	41.6%	5.50%
0.265	57.0%	19.4%	ND	18.7%	9.0%

SC represents *S. cerevisiae* and SP represent *S. pastorianus*. ND indicates permittivity values that were not obtainable.

TABLE II

COEFFICIENTS OF VARIATION OF $\Delta\varepsilon''$

Frequency (GHz)	SC Live	SC Dead	SP Live	SP Dead	5.5 µm
7.65	58.8%	52.1%	39.9%	44.8%	7.7%
5.55	39.6%	42.3%	35.8%	39.8%	23.2%
3.96	50.9%	58.8%	45.7%	33.9%	17.5%
2.38	43.6%	43.9%	43.9%	52.9%	24.4%
0.80	51.1%	119%	46.3%	ND	ND
0.265	44.5%	ND	40.7%	ND	ND

SC represents *S. cerevisiae* and SP represent *S. pastorianus*. ND indicates permittivity values that were not obtainable.

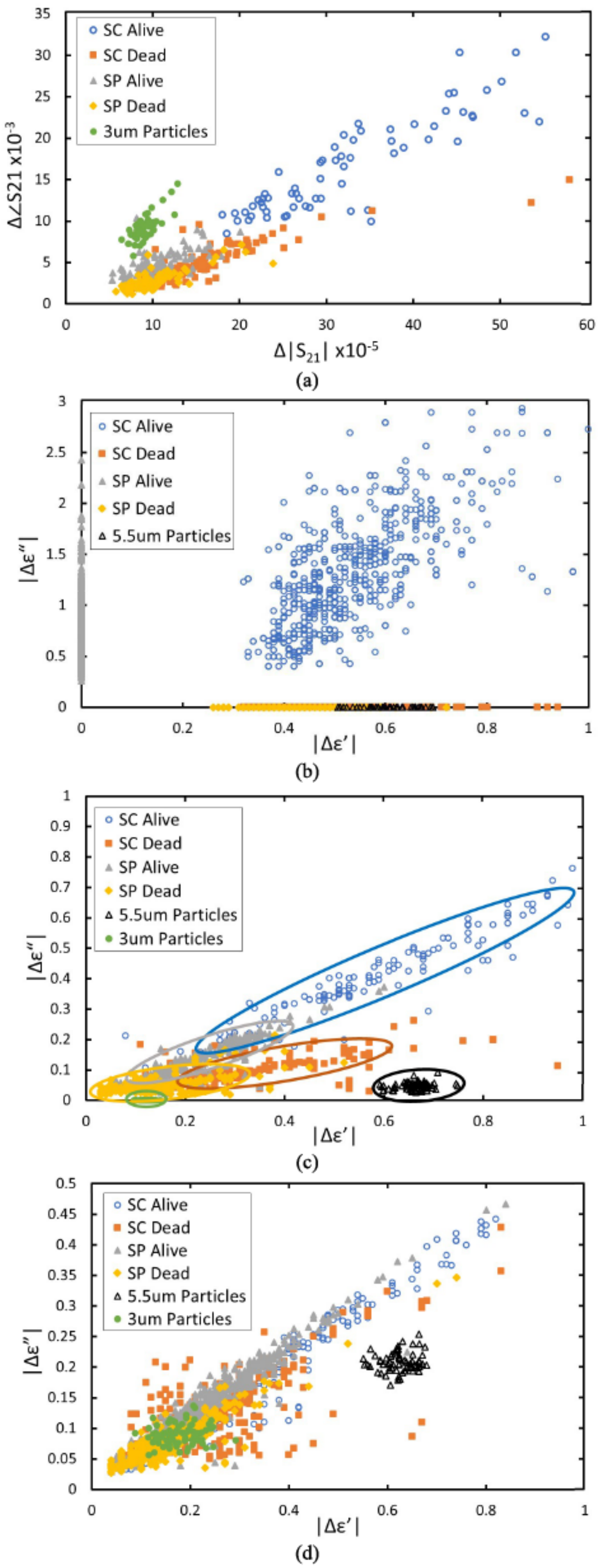

Fig. 12. (a) Scatter plot of the change in S_{21} magnitude versus phase at 2.38 GHz and scatter plots of permittivity of known samples at (b) 265 MHz, (c) 2.38 GHz, and (d) 7.65 GHz. Each data point represents the change in permittivity for a single cell or particle, with the *x*-axis being the real part and the y-axis the imaginary part. Note that there are no data for 3-μm particles at 265 MHz due to the inability to obtain a signal and the 5.5-μm particle data were left off (a) due to it having significantly larger values that would make the plot unreadable, caused by a lower minimum $|S_{21}|$ during measurements.

The results show that yeast signals have a significant distribution, which is quantified in Tables I and II. The distribution comes from various potential sources discussed above. Additionally, multiple cells passing through the sensor simultaneously or cells passing under the electrode in an area where there is no ground plane may have attributed in part to the variations, but from microscope observations during measurement, we estimate this occurring in less than 3% of measurements. Given the dilutions and the small areas without a ground plane relative to the areas that do contain a ground, the variations are mostly due to intrinsic differences between cells within the populations. Overall, viable *S. cerevisiae* has the largest distribution at the three frequencies, possibly due to larger microwave permittivity variations during the cell's life cycle compared to *S. pastorianus* cells. Further work is needed to understand the biological sources. All yeast signals and signal distributions are frequency-dependent. At higher frequencies, yeast permittivity values ($\Delta\varepsilon$) are lower, but the distributions remain constant. Different yeast species have different signals and permittivity values, which are also altered to different degrees by cell death. Though signal overlaps exist, there are significant separations at each frequency point. The differences indicate potential microwave specificity.

Fig. 13(a) and (b) shows the measured $\varepsilon^*_{\mathrm{MUT}}$ versus frequency with the water permittivity plotted for comparison. The extracted $\varepsilon^*_{\mathrm{MUT}}$ follows water permittivity trend, as is shown in bulk cell measurements [15]. Fig. 13(c) and (d) shows the trend of average yeast permittivity versus frequency.

At 265 MHz we see that the average value of $\Delta\varepsilon'$ for the two species of dead cells are smaller than the live counterparts. This is likely due to a decrease in membrane capacitance caused by cell death, since the membrane capacitance of yeast cells remains constant while the cells are viable and drops to zero at cell death, and a smaller membrane capacitance would be observed as a decrease in the real part of the cell's permittivity [30]. The difference observed between the two live species at the lowest frequency can also be described by differences in the cell's membrane capacitances, since the permittivity of yeast membranes has been shown to be correlated with flocculation abilities of yeast cell species, with weaker flocculating cells having a higher permittivity [31]. In this work, the authors observed that *S. cerevisiae* cells, which have a weaker flocculation ability than *S. pastorianus* cells, have a higher permittivity than *S. pastorianus* cells when measured in solution from 100 Hz to 100 kHz. The authors suggested the result was due to differences in cell surface charge between the two cell types, where a decrease in surface charge would decrease electrostatic repulsion between cells, and hence increase flocculation. However, a relationship between surface charge in yeast at the start of flocculation has not been found [46]. It has also been suggested that cell-surface hydrophobicity is responsible for flocculation in brewing yeast [47]. This is supported by measurements over the frequency range from 40 Hz to 110 MHz showing that the dielectric properties of the plasma membranes of live *S. cerevisiae* are strongly influenced by the properties of the hydrophobic layer of the cell membrane [48]. Regardless of the underlying mechanisms, our results are consistent with those reported in [31]. Although their measurements were performed at lower frequencies, the effects of membrane capacitance on permittivity have been observed at frequencies

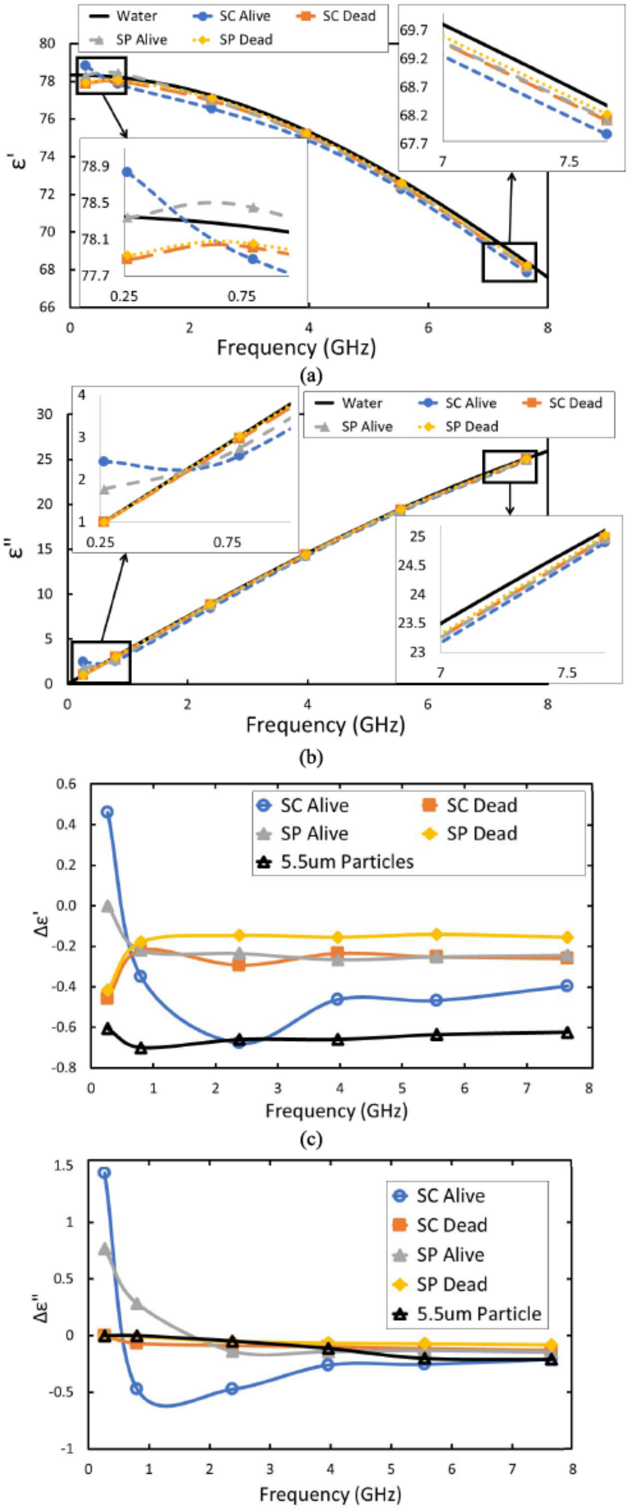

(a)

(b)

(c)

(d)

Fig. 13. Average shift of (a) ε' and (b) ε'' for the four cell classes versus frequency, with DI water as the baseline reference. The background reference was changed to water to help illustrate the differences observed between cell types. The media changes slightly between measurements based on chemical makeup and temperature. Efforts were made to keep the media as consistent as possible across measurements, minimizing the resulting error. (c) and (d) Average shift in (c) ε' and (d) ε'' versus frequency for each of the five mixture classes. The relative consistency in the 5.5-μm particle signals and the consistently large variability from cells across frequencies indicates that any observed frequency dependence is due to intrinsic cell properties.

as high as 100 MHz and are most likely the cause of our observations [34].

At frequencies 800 MHz and above, where microwave signals more readily probe structures within the cell membrane, it is possible that the difference observed between the two species is a result of *S. pastorianus* having a larger relative genome size (1.46) than *S. cerevisiae* (1.00) [36]. Regardless, due to the probing nature of high-frequency signals, several factors will influence measurements (nucleoplasm, cytoplasm, nucleus size, and nuclear envelope thickness) and thus further investigation is needed to verify this is the only cause.

The differences in $\Delta\varepsilon''$ observed between live and dead cells are likely due to increased membrane permeability caused by heat shock, meaning molecules in the external media can more readily diffuse across the cell membrane into the cell (and simultaneously, leakage of cytoplasmic ions) making the conductivity, and hence ε,″ inside the cell more closely match that of the media [33]. At the lowest frequency (265 MHz), this is supported by observations in [32], where the authors measured the dielectric properties of live and dead yeast cells in suspension from 60 to 600 kHz and observed lower dielectric loss ε'' of dead yeast suspensions compared to live cell suspensions. Despite these measurements being at lower frequencies than ours, the trend should extend to higher frequencies since at higher frequencies, penetration of the microwaves into the cell increases and cell membrane effects have little impact on the measured complex permittivity. This means intracellular differences between cells become more apparent. At frequencies of 800 MHz and above, where internal cell properties are more readily observed, our results are consistent with those in [20], where the authors observed by way of electrorotation a significant decrease in cytoplasmic conductivity in *S. cerevisiae,* from 5500 ± 500 to 100–800 μS/cm, when the cells were killed by heat shock. This decrease in conductivity would result in a smaller $\Delta\varepsilon''$ for dead cells compared to live cells, which is what we observed in our measurements.

This shift to internal cell properties being more readily observed at higher frequencies is apparent in the average $\Delta\varepsilon'$ at 800 MHz and above, where we see that live cells have a larger (more negative) shift than their dead counterparts. This is due to the protoplasm of the live yeast having a smaller permittivity than that of the media (which is mostly water) [16]. Again, due to the increased membrane permeability, the internal permittivity of the dead cells more closely resembles that of the media, while the permittivity of the live cell's protoplasm is much smaller, resulting in a larger shift for live cells. Additionally, the increase in $\Delta\varepsilon'$ above 265 MHz for dead cells can be explained by the membrane capacitance no longer having an observable effect.

C. Mixture Prediction

To better understand if microwave measurements can be exploited to discriminate yeast species and the viability of the yeast, a prediction model was developed using the measurement data described above. Quadratic discriminate analysis (QDA) was used for frequencies 2.38 GHz and above since the data obtained appear to have a normal distribution. K-nearest neighbor (KNN) was used for the lowest two frequencies due to having some data on only the x- or y-axis [Fig. 12(b)]. The training data consist of five classes—the four yeast classes (*S. cerevisiae* and *S. pastorianus*, live and dead) and 5.5-μm particles, which could represent debris in an application such as cell monitoring during fermentation, which would contain a significant amount of grain particulates from the mashing process that could potentially be misidentified as cells. Prediction models were developed and compared for individual frequencies. The exact sample data totals were 1351, 958, 1733, 842, 1493, and 1564 for the frequencies 7.65, 5.55, 3.96, 2.38, 0.800, and 0.265 GHz, respectively. The prediction algorithm, starting from raw S-parameter data, is shown in Fig. 14.

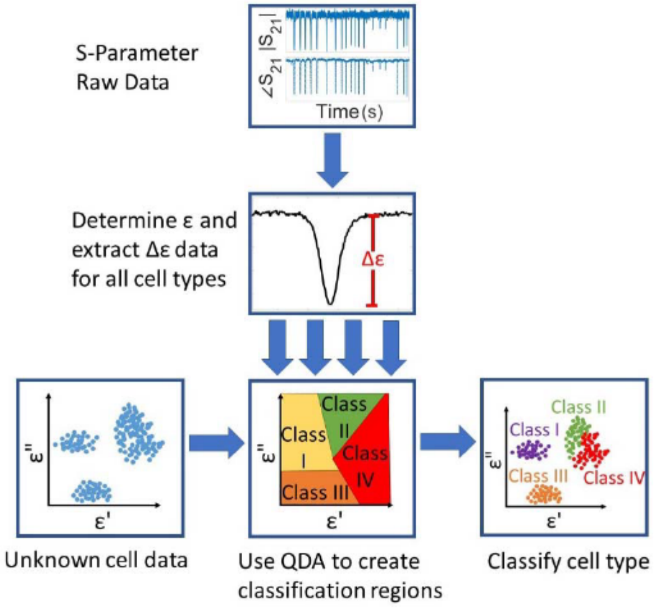

Fig. 14. Cell identification algorithm development. A quadratic classifier is used on known cell measurement data to create a decision surface. The regions on the surface can be used to classify unknown cell types in a mixture.

We found that 2.38 GHz and 265 MHz show the lowest uncertainty if using single-frequency measurements, with cross-validation errors of 27% and 15%, respectively, which supports the notion that certain frequencies are more sensitive to the minute differences between live and dead cells from the same species. It also suggests that broadband measurements of the same yeast cell should enhance the differentiation power.

To further test the sensing and prediction ability of the system in Fig. 1(b), the permittivity extraction algorithms in Fig. 5, and the models in Fig. 14, a mixture of the five classes is measured at each frequency point. The mixture contained equal parts of the four yeast classes (22.2% each) and half as many 5.5-μm particles (11.1%). Prior to mixing, cell densities were measured using a spectrophotometer. Fig. 15 shows typical time-domain measurement signals at 2.38 GHz.

At least 100 data points were collected at each frequency, the prediction results at each frequency are shown in Table III. While the cross-validation suggested that 265 MHz would be

TABLE III
PREDICTED CLASSIFICATIONS OF CELL MIXTURE

Frequency (GHz)	SC Live	SC Dead	SP Live	SP Dead	5.5 μm
7.65	25.6%	17.9%	23.9%	21.4%	11.1%
5.55	32.7%	18.3%	17.3%	15.4%	16.3%
3.96	9.4%	17.2%	32.8%	14.1%	26.6%
2.38	20.0%	21.8%	26.1%	22.4%	9.7%
0.80	44.1%	5.6%	6.3%	28.0%	16.1%
0.265	9.2%	35.9%	52.2%	0.0%	2.7%

the most accurate, the trained model is unable to distinguish between the two dead cell types and particles, all of which lie on the x-axis [Fig. 12(b)]. Fig. 16 shows the predicted classification of the mixture at 2.38 GHz, which agrees reasonably well with expectations. This further supports the statement that the slight differences in the media for the individual cell measurements discussed previously produce the minimal error, since that data were used for training the model.

The accuracy of predictions could be increased further by using larger training data sets or by using multifrequency measurements. In the case of multiple frequencies, decision trees could be used where differences are seen in only one or two classes at a frequency, such as *S. cerevisiae* and *S. pastorianus* live cells at 265 MHz, which can clearly be differentiated but the other classes have significant overlap.

IV. DISCUSSION

As shown in Fig. 12, significant distribution at every frequency is observed for each yeast class, with live *S. cerevisiae* having the largest. A major contributor to the variations comes from cells being in different stages of growth within the samples, since it is known that budding yeast and single yeast cells have different microwave dielectric behaviors [16]. Nevertheless, the variation between frequencies, shown in Tables I and II, is consistent, which indicates that the cell populations are uniform between frequency measurements. So, any observed frequency dependence reflects intrinsic cell property change versus frequency. With this assumption, there is a clear frequency dependence of both ε' and ε'' for all four cell classes, as is highlighted in Fig. 13, whereas the 5.5-μm particle responses are much more uniform. Furthermore, we see that the difference in $\Delta\varepsilon''$ is more significant at lower frequencies for the two live species while the difference of the dead cells remains roughly the same at all frequencies. The uniformity of the dead cell responses can be explained by the leakage of cytoplasmic ions resulting from membrane damage caused by heat shocking the cells to cause cell death. The more significant frequency dependence of the live cells is due to the cell membrane having a larger effect at the lowest frequency (β-dispersion), 265 MHz, while at higher frequencies the cell membrane has little impact on measurements, and instead differences between the permittivity of the cell protoplasm and that of the media are observed. Similar phenomena for $\Delta\varepsilon'$ is observed, except for a spike in *S. cerevisiae* live cells at 2.38 GHz, where the membrane capacitance plays a significant role at 265 MHz but has little effect at higher frequencies. The large $\Delta\varepsilon'$ observed in *S. cerevisiae* at 2.38 GHz is caused by a more drastic

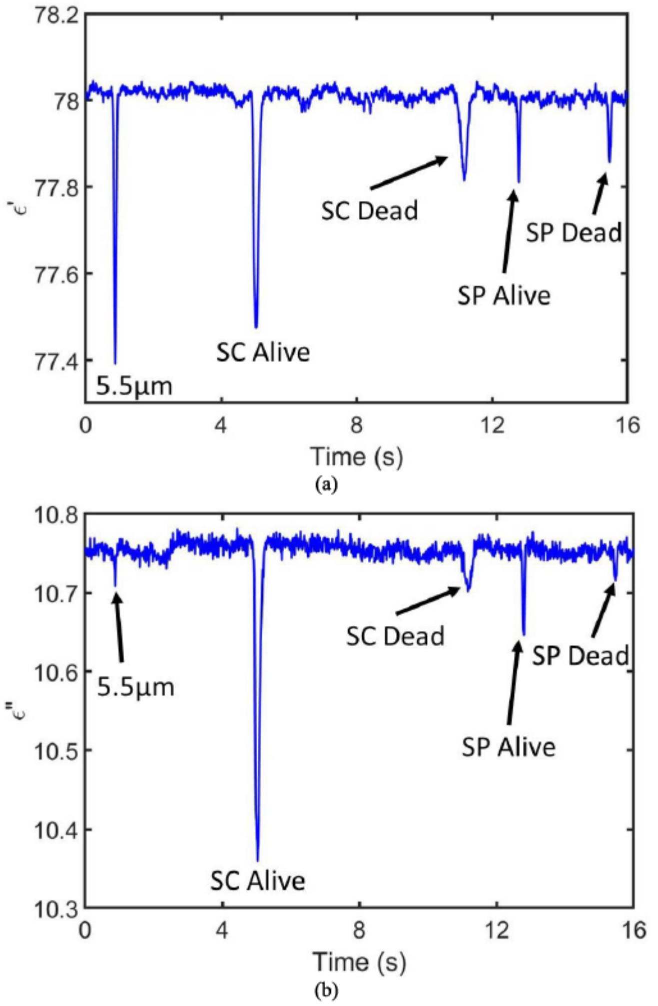

Fig. 15. Time-domain measurements of (a) ε' and (b) ε'' at 2.38 GHz showing typical signals for each of the five classes measured. Signal snippets were taken from known sample measurements and spliced together to demonstrate their differences.

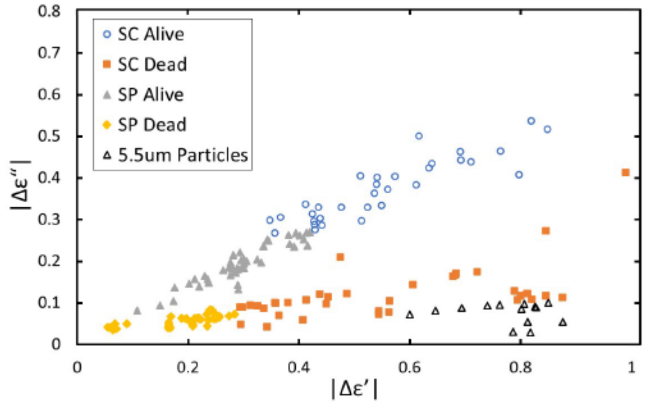

Fig. 16. Predicted classifications of mixture at 2.38 GHz. Predictions were made using QDA with the training data shown in Fig. 12(c).

difference between ε' of the protoplasm and ε' of the media, but the reason it occurs at this particular frequency is unknown.

The frequency-dependent properties make it difficult to compare the identification capabilities at higher frequencies with the two lowest frequencies, 800 and 265 MHz. For some of the yeast classes, we are only able to detect one of the permittivity values. Particularly at 265 MHz, where we only detect both ε' and ε'' for live *S. cerevisiae*. Due to this and the fact that live *S. pastorianus* is the only class where only ε'' is detectable, we can say that the differentiation of the two live species is solved at 265 MHz. However, for the remaining three classes we see that there is significant overlap to the point where we are unable to differentiate at all. Adding more classes at this frequency could lead to even worse performance. A similar trend is seen at 800 MHz, where we can detect ε' and ε'' for both live species but in roughly half of the dead cells we only see a signal for ε'. This may be in part due to the lower sensitivity of the sensor at low frequencies, where the minimum detectable signals are nearly 10 times larger than at higher frequencies. Improved sensitivity at low frequencies could lead to increased microwave specificity. While this may make it difficult to differentiate more cell classes at these isolated frequencies, it may be useful when developing multiple frequency measurement prediction models. For example, the lower frequencies could be used to detect viability and higher frequencies could differentiate between these closely related species.

This is further supported with the prediction models that were generated where we found that 2.38 GHz and 265 MHz had the lowest cross-validation errors. However, when the models were used to make predictions on cell mixtures, we were unable to differentiate between the two dead cells across the species, getting a 0% value for *S. pastorianus* dead and a significantly smaller than expected number of 5.5-μm particles. Additionally, it appears that a significant number of *S. cerevisiae* live cells were misclassified as *S. pastorianus* live. This is likely due to slight differences of the media in the mixture measurements from the media that was used for individual cell-type measurements. Other potential sources of errors include multiple cells passing under the electrode simultaneously, cells passing under the region of the microstrip for which there is no ground plane, and the vertical location of the cell in the channel. Future efforts will address these problems as well as concurrent multifrequency measurements of individual cells and minimizing sources of error.

V. CONCLUSION

In this work, we developed a microwave interferometer test platform for single yeast characterization. Using microstrip sensing structures, we showed that membrane differences in two yeast cell species, as well as two viability states, resulted in an observable differences in both the real and imaginary parts of the permittivity at 265 MHz. We also showed that increased permeability of the cell membrane in dead cells, induced by heat shock, resulted in lower permittivity inside the cells compared with live cells of the same species at 800 MHz and above. We were able to use these properties to differentiate between the two yeast species and determine their viability, as well as differentiate signals from PSPs from that of the cells.

We validated our measurements by creating prediction models at each frequency and testing them with mixtures containing live and dead cells from the two species and 5.5-μm particles. We found that of the frequencies we tested, 2.38 GHz has the highest degree of specificity, indicating that cells have a stronger frequency dependence than was previously known and that this frequency dependence can be exploited for microwave cell characterization measurements.

ACKNOWLEDGMENT

The authors would like to thank C. Ehrett and H. Smith for their discussions on discriminant analysis and guidance on creating the prediction model used in this article, and D. Czaplewski for his help with fabrication.

REFERENCES

[1] S. Afshar, E. Salimi, K. Braasch, M. Butler, D. J. Thomson, and G. E. Bridges, “Multi-frequency DEP cytometer employing a microwave sensor for dielectric analysis of single cells,” *IEEE Trans. Microw. Theory Techn.*, vol. 64, no. 3, pp. 991–998, Mar. 2016.

[2] A. Tamra, D. Dubuc, M.-P. Rols, and K. Grenier, “Microwave monitoring of single cell monocytes subjected to electroporation,” *IEEE Trans. Microw. Theory Techn.*, vol. 65, no. 9, pp. 3512–3518, Sep. 2017.

[3] H. Li *et al.*, “Differentiation of live and heat-killed E. Coli by microwave impedance spectroscopy,” *Sens. Actuators B, Chem.*, vol. 255, pp. 1614–1622, Feb. 2018.

[4] Y. Yang *et al.*, “Distinguishing the viability of a single yeast cell with an ultra-sensitive radio frequency sensor,” *Lab Chip*, vol. 10, no. 5, pp. 553–555, 2010.

[5] S. Gawad, L. Schild, and P. H. Renaud, “Micromachined impedance spectroscopy flow cytometer for cell analysis and particle sizing,” *Lab Chip*, vol. 1, no. 1, pp. 76–82, 2001.

[6] D. Holmes *et al.*, “Leukocyte analysis and differentiation using high speed microfluidic single cell impedance cytometry,” *Lab Chip*, vol. 9, no. 20, pp. 2881–2889, 2009.

[7] J. S. McGrath, C. Honrado, D. Spencer, B. Horton, H. L. Bridle, and H. Morgan, “Analysis of parasitic protozoa at the single-cell level using microfluidic impedance cytometry,” *Sci. Rep.*, vol. 7, no. 1, pp. 1–11, Jun. 2017.

[8] B. Slabbinck, B. De Baets, P. Dawyndt, and P. De Vos, “Towards large-scale FAME-based bacterial species identification using machine learning techniques,” *Systematic Appl. Microbiol.*, vol. 32, no. 3, pp. 163–176, May 2009.

[9] Y. Cui, J. Sun, Y. He, Z. Wang, and P. Wang, “A simple, tunable, and highly sensitive radio-frequency sensor,” *Appl. Phys. Lett.*, vol. 103, no. 6, Aug. 2013, Art. no. 062906.

[10] Y. Cui, W. F. Delaney, T. Darroudi, and P. Wang, “Microwave measurement of giant unilamellar vesicles in aqueous solution,” *Sci. Rep.*, vol. 8, no. 1, pp. 1–8, Jan. 2018.

[11] Z. Wang *et al.*, “Time domain detection and differentiation of single particles and cells with a radio frequency interferometer,” in *Proc. IEEE Topical Conf. Biomed. Wireless Technol., Netw., Sens. Syst. (BioWireleSS)*, Austin, TX, USA, Jan. 2016, pp. 77–80.

[12] C. Song, J. E. Harriss, and P. Wang, “Compensating on-chip transmission line losses for a high-sensitivity microwave sensor,” *Sens. Actuators A, Phys.*, vol. 154, no. 1, pp. 7–11, Aug. 2009.

[13] E. Yamashita and R. Mittra, “Variational method for the analysis of microstrip lines,” *IEEE Trans. Microw. Theory Techn.*, vol. MTT-16, no. 4, pp. 251–256, Apr. 1968.

[14] R. Crampagne, M. Ahmadpanah, and J.-L. Guiraud, “A simple method for determining the Green’s function for a large class of MIC lines having multilayered dielectric structures,” *IEEE Trans. Microw. Theory Techn.*, vol. MTT-26, no. 2, pp. 82–87, Feb. 1978.

[15] H. P. Schwan, “Electrical properties of tissues and cell suspensions: Mechanisms and models,” in *Proc. 16th Annu. Int. Conf. IEEE Eng. Med. Biol. Soc.*, Baltimore, MD, USA, vol. 1, Nov. 1994, pp. A70–A71.

[16] K. Asami and T. Yonezawa, "Dielectric behavior of wild-type yeast and vacuole-deficient mutant over a frequency range of 10 kHz to 10 GHz," *Biophys. J.*, vol. 71, no. 4, pp. 2192–2200, Oct. 1996.

[17] H. Zhu, M. Holl, T. Ray, S. Bhushan, and D. R. Meldrum, "Characterization of deep wet etching of fused silica glass for single cell and optical sensor deposition," *J. Micromech. Microeng.*, vol. 19, no. 6, Jun. 2009, Art. no. 065013.

[18] R. Garg, I. J. Bahl, and M. Bozzi, *Microstrip Lines and Slotlines*. Norwood, MA, USA: Artech House, 2013.

[19] A. K. Verma and G. H. Sadr, "Unified dispersion model for multilayer microstrip line," *IEEE Trans. Microw. Theory Techn.*, vol. 40, no. 7, pp. 1587–1591, Jul. 1992.

[20] R. Hölzel and I. Lamprecht, "Dielectric properties of yeast cells as determined by electrorotation," *Biochimica et Biophysica Acta (BBA)-Biomembranes*, vol. 1104, no. 1, pp. 195–200, Feb. 1992.

[21] Y.-F. Chen, H.-W. Wu, Y.-H. Hong, and H.-Y. Lee, "40 GHz RF biosensor based on microwave coplanar waveguide transmission line for cancer cells (HepG2) dielectric characterization," *Biosensors Bioelectron.*, vol. 61, pp. 417–421, Nov. 2014.

[22] M. Hussein, F. Awwad, D. Jithin, H. El Hasasna, K. Athamneh, and R. Iratni, "Breast cancer cells exhibits specific dielectric signature *in vitro* using the open-ended coaxial probe technique from 200 MHz to 13.6 GHz," *Sci. Rep.*, vol. 9, no. 1, pp. 1–8, Mar. 2019.

[23] K. Grenier, F. Artis, M. Poupot, J. Foumié, and D. Dubuc, "Label-free discrimination of human lymphoma cell sub-populations with microwave dielectric spectroscopy," in *IEEE MTT-S Int. Microw. Symp. Dig.*, Philadelphia, PA, USA, Jun. 2018, pp. 907–910.

[24] G. Qiao, W. Wang, W. Duan, F. Zheng, A. J. Sinclair, and C. R. Chatwin, "Bioimpedance analysis for the characterization of breast cancer cells in suspension," *IEEE Trans. Biomed. Eng.*, vol. 59, no. 8, pp. 2321–2329, Aug. 2012.

[25] Z. Macit, C. Aydinalp, T. Yilmaz, A. B. O. Sert, and F. N. Kok, "Microwave dielectric properties of osteosarcoma cell line (SAOS-2) suspensions," in *Proc. 23rd Int. Conf. Appl. Electromagn. Commun. (ICECOM)*, Dubrovnik, Croatia, Sep. 2019, pp. 1–4.

[26] A. Han, L. Yang, and A. B. Frazier, "Quantification of the heterogeneity in breast cancer cell lines using whole-cell impedance spectroscopy," *Clin. Cancer Res.*, vol. 13, no. 1, pp. 139–143, Jan. 2007.

[27] L. Ceriotti, J. Ponti, P. Colpo, E. Sabbioni, and F. Rossi, "Assessment of cytotoxicity by impedance spectroscopy," *Biosensors Bioelectron.*, vol. 22, no. 12, pp. 3057–3063, Jun. 2007.

[28] D. Opp, B. Wafula, J. Lim, E. Huang, J.-C. Lo, and C.-M. Lo, "Use of electric cell–substrate impedance sensing to assess *in vitro* cytotoxicity," *Biosensors Bioelectron.*, vol. 24, no. 8, pp. 2625–2629, Apr. 2009.

[29] J. P. Carvell and J. E. Dowd, "On-line measurements and control of viable cell density in cell culture manufacturing processes using radio-frequency impedance," *Cytotechnology*, vol. 50, nos. 1–3, pp. 35–48, Mar. 2006.

[30] P. Tibayrenc, L. Preziosi-Belloy, and C. Ghommidh, "On-line monitoring of dielectrical properties of yeast cells during a stress-model alcoholic fermentation," *Process Biochem.*, vol. 46, no. 1, pp. 193–201, Jan. 2011.

[31] D. Kregiel, J. Berlowska, and B. Szubzda, "Novel permittivity test for determination of yeast surface charge and flocculation abilities," *J. Ind. Microbiol. Biotechnol.*, vol. 39, no. 12, pp. 1881–1886, Dec. 2012.

[32] J. Yao, T. Kodera, A. Sapkota, H. Obara, and M. Takei, "Experimental study on dielectric properties of yeast cells in micro channel by impedance spectroscopy," in *Proc. Int. Symp. Micro-Nanomechatronics Human Sci. (MHS)*, Nagoya, Japan, Nov. 2014, pp. 1–4.

[33] A. Ebrahimi, L. N. Csonka, and M. A. Alam, "Analyzing thermal stability of cell membrane of salmonella using time-multiplexed impedance sensing," *Biophys. J.*, vol. 114, no. 3, pp. 609–618, Feb. 2018.

[34] R. Pethig and I. Schmueser, "Marking 100 years since Rudolf Höber's discovery of the insulating envelope surrounding cells and of the β-dispersion exhibited by tissue," *J. Elect. Bioimpedance*, vol. 3, no. 1, pp. 72–79, Jul. 2012.

[35] M. D. Janezic, D. F. Williams, V. Blaschke, A. Karamcheti, and C. S. Chang, "Permittivity characterization of low-k thin films from transmission-line measurements," *IEEE Trans. Microw. Theory Techn.*, vol. 51, no. 1, pp. 132–136, Jan. 2003.

[36] G. G. Stewart, "Saccharomyces," in *Encyclopedia of Food Microbiology*, C. A. Batt and M. L. Tortorello, Eds., 2nd ed. Burlington, MA, USA: Elsevier, 2014, pp. 297–315.

[37] G. I. de Becze, "A microbiological process report; yeasts. I. Morphology," *Appl. Microbiol.*, vol. 4, no. 1, pp. 1–12, Jan. 1955.

[38] M. Ciani, L. Canonico, L. Oro, and F. Comitini, "Footprint of nonconventional yeasts and their contribution in alcoholic fermentations," in *Biotechnological Progress and Beverage Consumption*, A. M. Grumezescu and A. M. Holban, Eds., 1st ed. Burlington, MA, USA: Elsevier, 2019, ch. 14, pp. 435–465.

[39] A. Querol, E. Barrio, and D. Ramón, "A comparative study of different methods of yeast strain characterization," *Systematic Appl. Microbiol.*, vol. 15, no. 3, pp. 439–446, Aug. 1992.

[40] R. Cody, "Saccharomyces cerevisiae and S. pastorianus species and strain differentiation by direct analysis in real time time-of-flight mass spectrometry," *Rapid Commun. Mass Spectrometry*, vol. 34, no. 17, p. e8835, May 2020.

[41] S. Torriani, G. Zapparoli, P. Malacrino, G. Suzzi, and F. Dellaglio, "Rapid identification and differentiation of saccharomyces cerevisiae, saccharomyces bayanus and their hybrids by multiplex PCR," *Lett. Appl. Microbiol.*, vol. 38, no. 3, pp. 239–244, Mar. 2004.

[42] K. P. Miller, Y. K. Gowtham, J. M. Henson, and S. W. Harcum, "Xylose isomerase improves growth and ethanol production rates from biomass sugars for both saccharomyces pastorianus and saccharomyces cerevisiae," *Biotechnol. Prog.*, vol. 28, no. 3, pp. 669–680, May 2012.

[43] S. M. G. Saerens, C. T. Duong, and E. Nevoigt, "Genetic improvement of brewer's yeast: Current state, perspectives and limits," *Appl. Microbiol. Biotechnol.*, vol. 86, no. 5, pp. 1195–1212, Mar. 2010.

[44] S. Guyot, P. Gervais, M. Young, P. Winckler, J. Dumont, and H. M. Davey, "Surviving the heat: heterogeneity of response in Saccharomyces cerevisiae provides insight into thermal damage to the membrane," *Environ. Microbiol.*, vol. 17, no. 8, pp. 2982–2992, Aug. 2015.

[45] P. Chen *et al.*, "Genome comparison and evolutionary analysis of different industrial lager yeasts (Saccharomyces pastorianus)," *J. Inst. Brewing*, vol. 122, no. 1, pp. 42–47, Jan. 2016.

[46] P. B. Dengis, L. R. Nélissen, and P. G. Rouxhet, "Mechanisms of yeast flocculation: Comparison of top- and bottom-fermenting strains," *Appl. Environ. Microbiol.*, vol. 61, no. 2, pp. 718–728, 1995.

[47] E. V. Soares, "Flocculation in saccharomyces cerevisiae: A review," *J. Appl. Microbiol.*, vol. 110, no. 1, pp. 1–18, Jan. 2011.

[48] M. Stoneman, A. Chaturvedi, D. B. Jansma, M. Kosempa, C. Zeng, and V. Raicu, "Protein influence on the plasma membrane dielectric properties: *In vivo* study utilizing dielectric spectroscopy and fluorescence microscopy," *Bioelectrochemistry*, vol. 70, no. 2, pp. 542–550, May 2007.